ADVANCED OPTICAL MATERIALS
www.advopticalmat.de

Check for updates

Nonvolatile Multilevel Switching of Silicon Photonic Devices with In_2O_3/GST Segmented Structures

Changping Zhang, Maoliang Wei, Jun Zheng, Shujun Liu, Hongyuan Cao, Yishu Huang, Ying Tan, Ming Zhang, Yiwei Xie, Zejie Yu, Junying Li, Hui Ye, Lan Li, Hongtao Lin, Huan Li, Yaocheng Shi, Liu Liu, and Daoxin Dai**

Reconfigurable silicon photonic devices are widely used in numerous emerging fields such as optical interconnects, photonic neural networks, quantum computing, and microwave photonics. Currently, phase change materials (PCMs) have been extensively investigated as promising candidates for building switching units due to their strong refractive index modulation. Here, nonvolatile multilevel switching of silicon photonic devices with $Ge_2Sb_2Te_5$ (GST) is demonstrated with In_2O_3 transparent microheaters that are compatible with diverse material platforms. With GST integrated on the silicon photonic waveguides and Mach-Zehnder interferometers (MZIs), repeatable and reversible multilevel modulation of GST is achieved by electro-thermally induced phase transitions. Particularly, the segmented switching unit of In_2O_3 and GST is proposed and demonstrated to be capable of producing about one order of magnitude larger temperature gradient than that of the nonsegmented unit, resulting in up to 64 distinguishable switching levels of 6-bit precision, and fine-tuning of the switching voltage pulses is promising to push the precision even further, to 7-bit, or 128 distinguishable switching levels. The capability of precise multilevel phase-change modulation is crucial to further facilitate the development of nonvolatile reconfigurable switches and variable attenuation devices as building blocks in large-scale programmable optoelectronic systems.

1. Introduction

Silicon photonics, due to its unique advantages such as high integration density and complementary-metal-oxide-semiconductor (CMOS) compatibility, has not only been used in conventional communication and signal processing systems, but also exhibited great potential for various important applications in emerging fields such as Internet of Things, artificial intelligence, and quantum computing.[1–3] Reconfigurable photonic integrated devices and circuits can perform functions such as switching, routing, and programming control of optical signals, thus are under extensive research and development. In order to further improve the performances and meet more stringent application requirements, it is crucial to realize large-scale silicon photonic integrated circuits, while ensuring compact device sizes and low power consumption. The conventional silicon photonic switching in reconfigurable systems mainly utilizes the thermo-optic (TO) effects[4,5] or carrier-induced electro-optic (EO) effects[6,7] to change the refractive index of the material, thereby providing a phase shift during light transmission. However, the phase shift provided by these schemes is usually small, and the sizes of the devices are relatively large, which is not conducive to large-scale photonic integration. In addition, the switching processes of such conventional photonic devices are volatile and

C. Zhang, J. Zheng, S. Liu, H. Cao, Y. Huang, Y. Tan, M. Zhang, Y. Xie, Z. Yu, H. Ye, H. Li, Y. Shi, L. Liu, D. Dai
State Key Laboratory for Modern Optical Instrumentation
Center for Optical & Electromagnetic Research
College of Optical Science and Engineering
International Research Center for Advanced Photonics
Zhejiang University
Zijingang Campus, Hangzhou 310058, P. R. China
E-mail: lihuan20@zju.edu.cn; dxdai@zju.edu.cn

M. Wei, J. Li, H. Lin
State Key Laboratory of Modern Optical Instrumentation
College of Information Science and Electronic Engineering
Zhejiang University
Hangzhou 310027, P. R. China

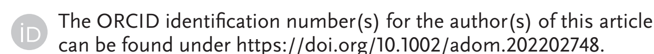
The ORCID identification number(s) for the author(s) of this article can be found under https://doi.org/10.1002/adom.202202748.

Y. Tan, M. Zhang, Y. Shi, D. Dai
Ningbo Research Institute
Zhejiang University
Ningbo 315100, P. R. China

L. Li
Key Laboratory of 3D Micro/Nano Fabrication and Characterization of Zhejiang Province
School of Engineering
Westlake University
Hangzhou 310024, P. R. China

L. Li
Institute of Advanced Technology
Westlake Institute for Advanced Study
Hangzhou, Zhejiang 310024, P. R. China

DOI: 10.1002/adom.202202748

 © 2023 Wiley-VCH GmbH

require constant energy supplies, resulting in considerable power consumption.

Phase-change materials (PCMs), such as $Ge_2Sb_2Te_5$ (GST), can produce a drastic change in their optical properties when transitioning between the amorphous and crystalline states.[8] Therefore, the integration of the PCMs on the silicon-on-insulator (SOI) platform enables high-contrast switching within a relatively short length of the switching unit. Meanwhile, the nonvolatility of the PCMs implies that power consumption is required only during the phase transition process and no power is consumed to maintain the state, which is suitable for building on-chip reconfigurable multifunctional photonic processors, where reconfigurations are not frequently required, such that the power consumption can be extremely low.[9] Numerous research works have shown that PCMs are promising for crucial applications in the fields of optical switching,[10–16] optical memory,[17–21] optical computing,[22–24] and photonic neural networks.[25–28] GST is one of the most promising and extensively investigated PCMs for integration with silicon photonics.[29,30] A 16×16 array of on-chip matrix multiplication network using GST-based directional coupler switches has been demonstrated for large-scale photonic in-memory computing.[27] More recently, a multilevel optical memristive switch based on a silicon Fabry–Perot resonator with GST has also been realized, which exhibits a maximum transmission contrast of 10.29 dB and 38 distinct switching levels.[16]

Currently, reversible phase transitions of phase change materials are mainly achieved by suitable optically or electrically provided heat stimuli.[31] More specifically, the amorphization is achieved by heating GST above its melting point (≈600 °C) and then quenching it rapidly to the disordered glass state. For crystallization, GST should be heated just above the glass transition temperature (≈150 °C) but below the melting point with a relatively low power for a long time (hundreds of nanoseconds) to enable nucleation and subsequent growth of the crystals.[32,33] On-chip all-optical switching via evanescent field absorption induces phase changes through pump light inside PCM-loaded waveguides.[17–28] The phase transition structure of this scheme is relatively simple, but the absorption of light is weak when the PCM is in the low-loss amorphous state, which hinders complete crystallization in a large area. Waveguide crossings and additional grating couplers are usually needed to guide the pump light in the photonic networks, leading to a limited integration density. Similar to phase-change random access memories (PRAM), the phase transition can be induced by Joule heating generated from electrical currents directly passing through the PCMs.[34,35] The crystallization of this mechanism may be compromised by the phenomenon known as "filamentation", which leads to nonuniform crystallization over hundreds of nanometers.[36]

For the sizes of PCMs which are usually on the wavelength scale in photonic applications, electrical switching using external resistive heaters is suitable for achieving uniform phase change in large-scale arrays with increased integration density and does not require the sophisticated excitation or alignment processes in the optical switching scheme. The heaters are based on doped silicon,[13,16,37,38] silicon PIN diode,[15,39] graphene,[40,41] and indium tin oxide (ITO).[11,42–44] As for the doping scheme that has been widely investigated recently, ridge waveguides are required, resulting in increased heat capacity and conductivity, hence higher power consumption. In addition, the applications of doped-silicon microheaters are only feasible for SOI platform and cannot be adopted by other material systems such as silicon nitride (SiN). Using graphene as external heaters can effectively reduce the phase change power consumption due to its high thermal and electrical conductivity, but the device yield for large-scale fabrication is still quite a challenge. Meanwhile, rapid progress have been made for ITO microheaters. A GST-loaded Mach-Zehnder interferometer (MZI) on SiN with ITO microheaters has been demonstrated to realize a 50° reconfigurable phase shift and seven crystallization steps.[44] Regardless of the specific microheater implementation, achieving amplitude and phase tuning with a wider range and a higher precision is challenging but of great importance, which requires multistage phase transitions. In this regard, electro-thermally induced multilevel switching including five stages has been reported with multimode interferometers (MMIs) in 2019,[13,37] and 5-bit precision has been realized with resistive heaters based on doped silicon.[16] In addition, using doped-silicon microheaters with "bridges", a single-step partial amorphization scheme with around ten intermediate states is demonstrated.[38]

In this work, we demonstrate repeatable and reversible multi-stage phase transitions of GST between the crystalline and amorphous states induced electro-thermally by using the resistive heater based on transparent conductive oxides (TCOs) In_2O_3, which are compatible with diverse material platforms. The In_2O_3/GST segmented structure is proposed and demonstrated to enable the capability of multistage phase transitions of a long GST strip (≈10 µm). In the present case, the maximum temperature gradient of GST for the segmented heating is ≈6-times higher than that for the nonsegmented heating, producing up to 64 distinguishable switching levels (corresponding to 6 bits), and even 128 levels can be realized with fine control of switching pulses. Utilizing GST-loaded silicon photonic waveguides in MZIs, it is shown that the loss contrast between the amorphous and crystalline states of GST is ≈1 dB μm^{-1}, and the phase shift induced by the change in the real part of refractive index is ≈0.04 $\pi\ \mu m^{-1}$. The proposed microheater architecture for inducing the phase transitions of PCMs is widely applicable, versatile, and scalable for switches and attenuators.

2. Experimental Section

2.1. Device Fabrication

The devices were fabricated on the SOI platform with a 220-nm-thick silicon layer on top of a 2-µm-thick buried oxide layer. For the silicon photonic waveguides, the pattern was formed by electron-beam lithography (EBL) with negative-tone resist (maN-2403). After that, the inductively coupled plasma reactive ion etching (ICP-RIE) was utilized to fully etch the silicon core layer. Another EBL lithography followed by a 70-nm shallow etching was performed to fabricate the grating couplers used for chip-fiber coupling. Next, a positive-tone resist (PMMA) was spin-coated and a third EBL was performed to pattern the GST deposition window on the silicon core. A 15-nm GST layer was

© 2023 Wiley-VCH GmbH

21951071, 2023, 8, Downloaded from https://onlinelibrary.wiley.com/doi/10.1002/adom.202202748 by Westlake University, Wiley Online Library on [05/07/2023]. See the Terms and Conditions (https://onlinelibrary.wiley.com/terms-and-conditions) on Wiley Online Library for rules of use; OA articles are governed by the applicable Creative Commons License

21951071, 2023, 8, Downloaded from https://onlinelibrary.wiley.com/doi/10.1002/adom.202202748 by Westlake University, Wiley Online Library on [05/07/2023]. See the Terms and Conditions (https://onlinelibrary.wiley.com/terms-and-conditions) on Wiley Online Library for rules of use; OA articles are governed by the applicable Creative Commons License

deposited through thermal evaporation followed by a lift-off process. Then, a 50-nm-thick In_2O_3 layer was sputtered without oxygen gas flow and lifted off after another EBL process. Subsequently, the In_2O_3 thin film was annealed at 300 °C for 60 mins under vacuum $<5 \times 10^{-3}$ Pa to lower the optical loss and improve the film stability. Finally, a stack of metal layers composed of 10-nm-thick Ti adhesion layer and 100-nm-thick Au layer were electron-beam evaporated to contact with the In_2O_3 thin film. The atomic percentages of Ge, Sb, and Te in the as-deposited GST thin film are 24%, 22%, and 54%, respectively, measured with energy dispersion spectroscopy (EDS). Meanwhile, the atomic percentages of In and O in the In_2O_3 thin film are 14% and 86%, respectively, also measured with EDS. The significantly higher percentage of O atoms is attributed to direct air exposure during the device measurement.

2.2. Device Modeling and Simulation

The spatial and temporal temperature responses of the device were investigated by the coupled electro-thermal three-dimensional (3D) finite-element-method (FEM) simulations using COMSOL Multiphysics. In the simulation, the Heat Transfer in Solids module and electric currents module combined with electromagnetic heating were employed to calculate the temperature distribution.

In the Heat Transfer in Solids module, the bottom boundary of the silicon substrate was assumed to keep a constant room temperature of T = 300 K, while the convective heat flux boundary condition was used on the top surface with a heat transfer coefficient of 5 W $(m^2 \cdot K)^{-1}$. Thermally insulating boundary conditions were adopted on the rest of the model boundaries. The simulation domain is sufficiently large to ensure that the temperature at these boundaries is nearly constant at room temperature. In the electric currents module, electrically insulating boundary conditions were applied to all the external boundaries except for the two edges of the In_2O_3 layer across the silicon waveguide, which were used for applying voltage pulses and grounding, respectively. The thermal and electrical properties of the materials used in the simulation are tabulated in **Table 1**.

Table 1. Thermal and electrical properties of the materials used in the FEM simulation.

Material	Thermal conductivity [W m^{-1} K^{-1}]	Heat capacity [J kg^{-1} K^{-1}]	Density [kg m^{-3}]	Electrical conductivity [S m^{-1}]
Si	149	720	2329	1×10^2
SiO_2	1.38	740	2203	1×10^{-14}
aGST	0.19	213	5870	40
cGST	0.57	199	6270	2×10^3
In_2O_3	11	340	7100	6×10^4

3. Structure Design

Using In_2O_3 transparent electrodes as resistive microheaters, Joule heat is generated by applying voltage pulses and thus the temperature of GST is changed to induce the phase transition. As illustrated in **Figure 1**a, a 15-nm-thick GST layer is deposited on the fully-etched 220-nm-thick silicon core. Then a 50-nm-thick In_2O_3 layer is deposited across the GST and the silicon core, acting as a resistive heater and also a protective layer. Electrodes composed of a 10/100-nm-thick Ti/Au layer are then deposited over the edges of the In_2O_3 layer to form ohmic contacts. The In_2O_3 heating region is divided into multiple segments to achieve multi-stage phase transitions and high-contrast switching. Figure 1a-c shows the schematic structure

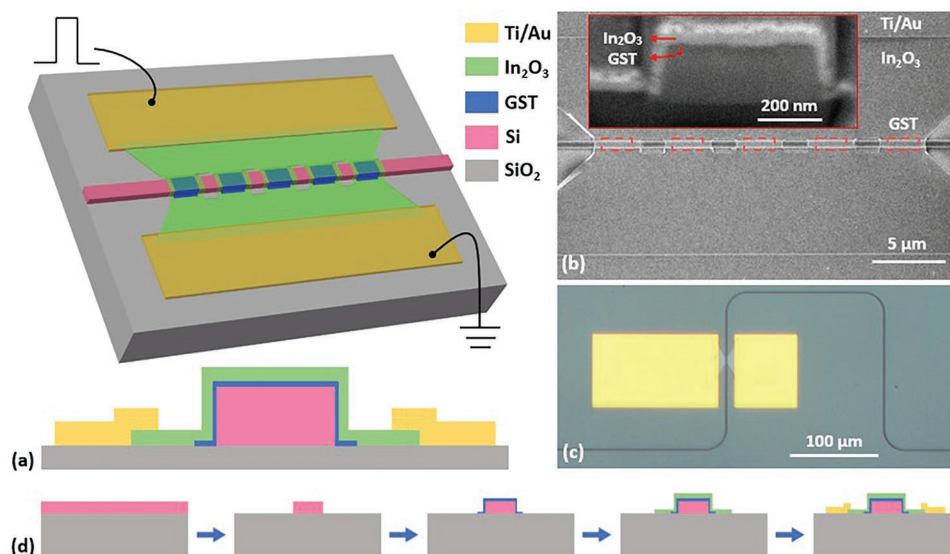

Figure 1. Schematic structure of the nonvolatile electro-thermally reconfigurable photonic switching unit. a) Top view and cross-section of the device. b) SEM image of the segmented In_2O_3 heating region. The inset SEM image shows the GST-loaded waveguide cross-section, tilted at 45°. c) Optical microscope image of the fabricated switching unit. d) The fabrication process of the switching unit.

 © 2023 Wiley-VCH GmbH

21951071, 2023, 8, Downloaded from https://onlinelibrary.wiley.com/doi/10.1002/adom.202202748 by Westlake University, Wiley Online Library on [05/07/2023]. See the Terms and Conditions (https://onlinelibrary.wiley.com/terms-and-conditions) on Wiley Online Library for rules of use; OA articles are governed by the applicable Creative Commons License

and the scanning electron microscope (SEM) and optical microscope images of the electro-thermally reconfigurable switching unit, which employs a 3-µm-long In_2O_3 and 2-µm-long GST thin-films for each segment. There are 5 segments in total and a 2-µm-long spacing between adjacent segments. The inset of Figure 1b shows the SEM image of the GST-loaded waveguide cross-section, prepared with a focused ion beam (FIB). The GST and In_2O_3 films above the silicon waveguide are marked in the image. Note that the bright film at the top surface is the sputtered gold, which is used to increase the sample conductivity for SEM observation. Figure 1d shows the fabrication process of the switching unit (see Experimental Section for more details).

The In_2O_3 thin film used in this scheme has acceptable absorption of light ($k \approx 0.015$) in the telecom band, and its real part of refractive index ($n \approx 2$) is relatively low compared with silicon and GST, which only slightly perturbs the optical mode when directly deposited on top of the silicon core. Meanwhile, the In_2O_3 thin film readily encapsulates the GST, such that the Joule heat generated therein can be rapidly conducted to GST, enabling rapid quenching and annealing processes for amorphization and crystallization, respectively. In addition, the In_2O_3 thin film can simultaneously serve as a protective layer against oxidation of GST due to air exposure and degradation during the phase transition cycles,[11,45] eliminating the need for additional fabrication processes for GST encapsulation.

Figure 2a shows the simulated temperature distribution at the top of the switching unit immediately after the application of a short voltage pulse, which is obtained by FEM simulations using COMSOL Multiphysics (see Experimental Section for the detailed simulation setup). The temperature rise is mostly confined within the In_2O_3 heating region due to the high thermal conductivity of the metal electrodes, which are almost clamped to room temperature. Figure 2b shows the temperature distribution at the silicon-GST interface, indicated by the dashed line in Figure 2a, when the rectangular voltage pulse energy is varied from 80 nJ to 120 nJ. Evidently, when the pulse energy is gradually increased, the temperature distribution along the waveguide rises proportionally. Furthermore, when the segmented heating structure is used, a temperature gradient can be established within each segment. Although the actual phase-change processes may be much more complicated than our semi-quantitative model below, we believe the large temperature gradient is the key to high-precision multi-stage phase transitions experimentally demonstrated later in this work.

Consider the amorphization process of fully crystalline GST segments. As the peak temperature after the switching pulse just reaches the GST melting point, the quenching and amorphization occur only in the middle of each GST segment. Define the switching pulse energy in this case as $Q_{\min}$. As the pulse energy and the peak temperature increase, the quenching and amorphization gradually expand from the middle to both ends of the GST. Eventually, complete amorphization can be achieved when the temperature of the entire GST segment is just higher than the melting point. Define the switching pulse energy in this case as $Q_{\max}$. Then the total number of multi-stage phase transitions $M \leq \Delta Q/\delta Q$, where $\Delta Q = Q_{\max} - Q_{\min}$ is the energy swing of the switching pulse and δQ is the minimum increment of the switching pulse energy, determined by the experimental setup. Therefore, a larger temperature gradient generally leads to larger energy

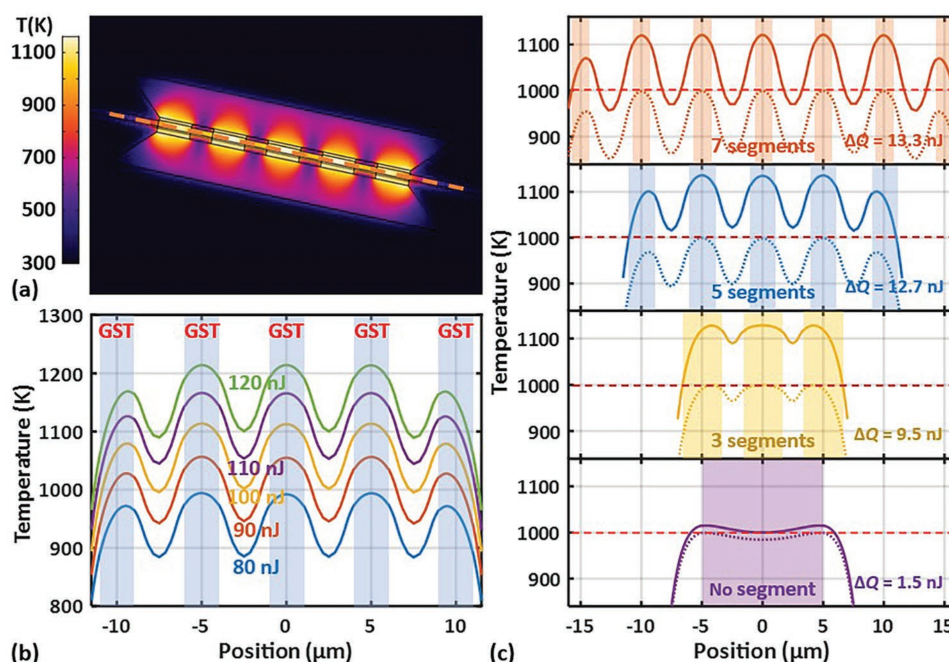

Figure 2. a) Temperature profile simulation of the In_2O_3 microheater consisting of 5 segments, each with a 2-µm-long GST. b) Simulated longitudinal temperature distribution of GST along the waveguide obtained by COMSOL Multiphysics as the pulse energy varies. c) Comparison of the temperature distributions between the nonsegmented and segmented heating with 3, 5, and 7 segments, for which the total lengths of GST are kept the same (10 µm). The shaded regions indicate the GST locations for the nonsegmented and segmented heating, respectively.

 © 2023 Wiley-VCH GmbH

swing (ΔQ), hence more stages of phase transitions (M), as further illustrated below.

Without loss of generality, assuming the melting point of GST is 1000 K, Figure 2c shows the comparison of nonsegmented and segmented heating, for which the total lengths of GST are kept to be the same (10 µm). The four subplots in Figure 2c correspond to different switching units with 1 (nonsegmented), 3, 5, and 7 segments. In each case, the temperature distributions for switching pulses of Q_{max} (solid lines) and Q_{min} (dotted lines) are shown, with ΔQ = 1.5, 9.5, 12.7, and 13.3 nJ for 1, 3, 5, and 7 segments, respectively. Meanwhile, the maximum temperature gradients of the center GST segments are calculated to be 5.4, 11.4, 33, and 33.3 K μm^{-1} for 1, 3, 5, and 7 segments, respectively, which indicates that the maximum temperature gradient of GST for the 5-segmented heating in our design is ≈6-times higher than that for the nonsegmented heating. As the number of segments increases to 7, there is no significant improvement for the maximum temperature gradient of GST due to the shorter length of each segment, while high-quality film growth and lift-off processes in the fabrication become challenging. Nevertheless, when the total length of GST increases, more intermediate states can be achieved by increasing the number of segments accordingly due to the higher switching contrast that can be provided. Therefore, the present segmented heating with 5 segments facilitates the generation of more intermediate states, leading to more precise multi-stage phase transitions than the conventional nonsegmented heating.

4. Measurement

In order to investigate the loss contrast caused by the phase change of GST, we integrate the segmented switching unit on a singlemode waveguide. The absorption loss of the GST is changed due to the phase change, leading to modulated optical transmission of the GST-loaded waveguide. The schematic structure of the switching unit and the SEM image are shown in **Figure 3**a. The GST is in the lossy crystalline state initially, exhibiting a high transmission loss.

To induce phase changes, we applied the voltage pulses to the metal electrodes with a pair of RF probes, so as to maintain the signal integrity. The actual switching energy is determined by the pulse amplitude, the pulse width, and the resistance. The resistance varies slightly from device to device even with the same switching-unit design due to fabrication variations. To achieve amorphization, the GST thin film should be heated above its melting point and quenched rapidly, for which we applied a voltage pulse with high amplitude and narrow width. For this fabricated device (with a resistance of ≈0.4 kΩ), amorphization occurs when a 1 µs voltage pulse of 7 V is applied, resulting in decreased waveguide loss and increased transmission. As the amplitude and width of the pulse increase, the transmission rises gradually. When a 2.8 µs voltage pulse of 8 V is applied, the transmission reaches the maximum, indicating that all GST segments of the device have been changed into the amorphous state. To achieve crystallization, GST should be heated above its glass transition temperature but below its

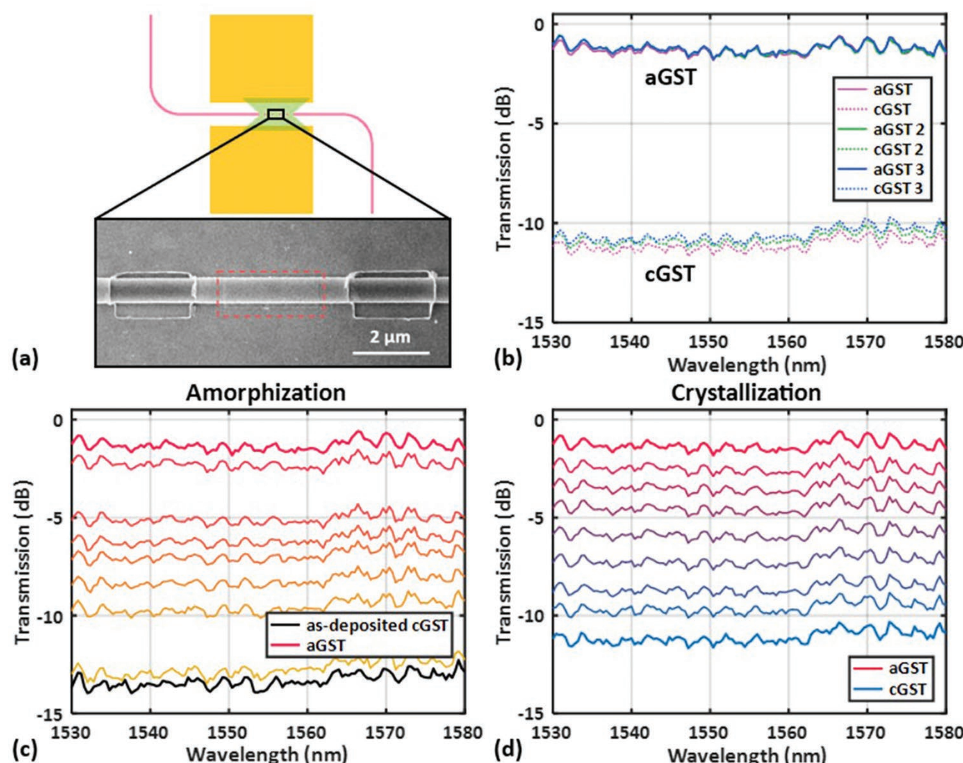

Figure 3. a) Schematic structure of the switching unit and the enlarged SEM image of the In_2O_3 heating region. b) Transmission spectra during several complete phase transitions of GST. Transmission levels of multi-stage c) amorphization and d) crystallization process of GST when different voltage pulses are applied. aGST (cGST): amorphous (crystalline) GST.

© 2023 Wiley-VCH GmbH

21951071, 2023, 8, Downloaded from https://onlinelibrary.wiley.com/doi/10.1002/adom.202202748 by Westlake University, Wiley Online Library on [05/07/2023]. See the Terms and Conditions (https://onlinelibrary.wiley.com/terms-and-conditions) on Wiley Online Library for rules of use; OA articles are governed by the applicable Creative Commons License

ADVANCED OPTICAL MATERIALS
www.advopticalmat.de

melting point and then annealed slowly. For this phase change, we apply a wide voltage pulse with low amplitude. When a 4 µs pulse with a voltage of 5 V is applied, crystallization occurs, resulting in increased waveguide loss and decreased transmission. As the pulse amplitude and the pulse width increase, the transmission drops gradually. When a 100 µs voltage pulse of 6 V is applied, the transmission reaches the minimum, indicating that all GST segments have been converted into the crystalline state.

The transmission exhibits excellent consistency after several complete cycles of phase transitions, as shown in Figure 3b. During the crystallization process, the applied voltage amplitude should not be too high. Otherwise, it may cause the GST temperature to reach its melting point, resulting in the amorphization process instead. Figure 3c-d shows the multistage amorphization and crystallization processes of GST when different voltage pulses are applied. It shows different transmission levels corresponding to different GST states, which demonstrates the multilevel-switching capability. Several cycles of amorphization/crystallization processes were performed for the device, and the measured transmission contrast is ≈10 dB for 10-µm-long GST segments. Correspondingly, the loss contrast is ≈1 dB μm^{-1}.

By integrating the segmented switching unit on a 1 × 1 imbalanced MZI, the phase and loss differences between two MZI arms can be fine-tuned. The schematic structure of the device is shown in **Figure 4**a. The two MZI arms are singlemode and the waveguide width is ≈500 nm, while the length difference between the two arms is 100 µm.

For this device (≈1.1 kΩ), amorphization is induced when a 1.1 µs voltage pulse of 9 V is applied, which corresponds to an increase in the extinction ratio (ER) and red shift of the MZI transmission spectrum. Keeping the voltage amplitude constant and gradually increasing the pulse width to 1.8 µs, the ER reaches the maximum of ≈20 dB with an excess loss (EL) ≈1 dB, indicating that the GST segments in the device has been changed completely into the amorphous state. As for the crystallization, when a 5 µs voltage pulse of 6 V was applied, the crystallization process is induced with a blue shift and a decrease in the ER of the transmission spectrum. As the pulse width is increased to 60 µs with a fixed pulse amplitude at 6 V, the ER reaches the minimum of ≈5 dB and the EL is ≈4 dB, indicating that all GST segments have been changed to the crystalline state.

The device was also tested under several complete cycles of phase transitions as mentioned above. The measurement results are illustrated in Figure 4b, which exhibit excellent consistency as well. Figure 4c-d shows the multistage amorphization and crystallization processes of GST, presenting different levels of ER and EL in the transmission spectra. Through the simulation and fitting of the respective transmission spectra, the waveguide loss is ≈0.15 dB μm^{-1} for amorphous GST and ≈1.2 dB μm^{-1} for crystalline GST. The loss contrast of ≈1 dB μm^{-1} is consistent with the measurement result from Figure 3b.

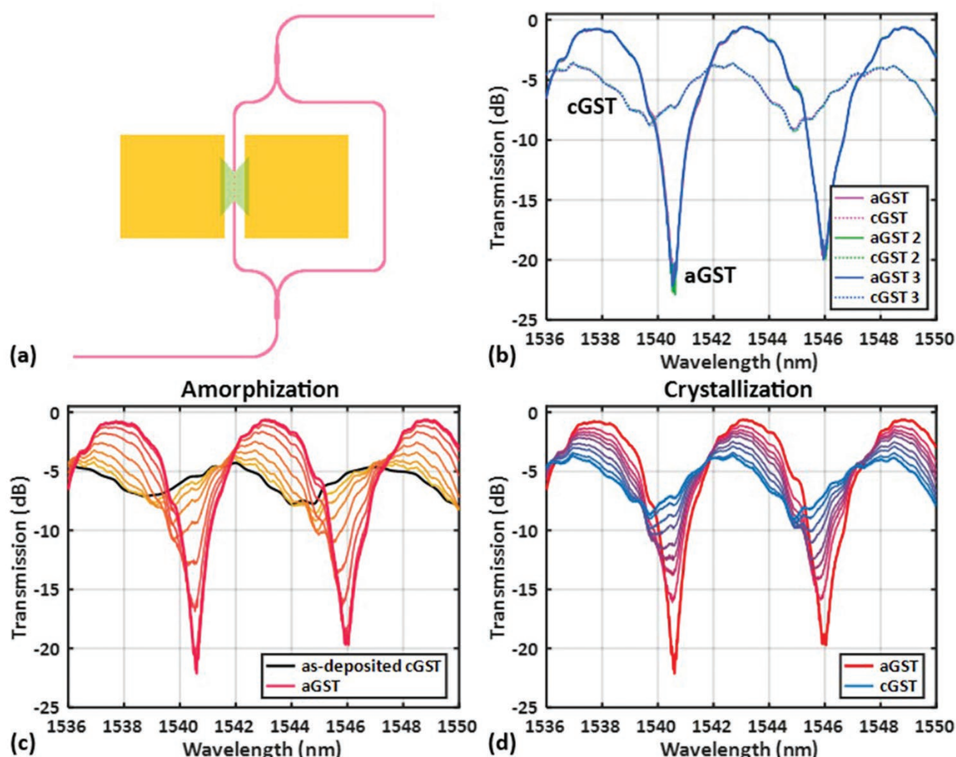

Figure 4. a) Schematic structure of the switching unit on the 1 × 1 imbalanced MZI. b) Transmission spectra during several complete phase transitions of GST. Transmission levels of multistage c) amorphization and d) crystallization process of GST when different voltage pulses are applied. aGST (cGST): amorphous (crystalline) GST.

© 2023 Wiley-VCH GmbH
21951071, 2023, 8, Downloaded from https://onlinelibrary.wiley.com/doi/10.1002/adom.202202748 by Westlake University, Wiley Online Library on [05/07/2023]. See the Terms and Conditions (https://onlinelibrary.wiley.com/terms-and-conditions) on Wiley Online Library for rules of use; OA articles are governed by the applicable Creative Commons License

21951071, 2023, 8, Downloaded from https://onlinelibrary.wiley.com/doi/10.1002/adom.202202748 by Westlake University, Wiley Online Library on [05/07/2023]. See the Terms and Conditions (https://onlinelibrary.wiley.com/terms-and-conditions) on Wiley Online Library for rules of use; OA articles are governed by the applicable Creative Commons License

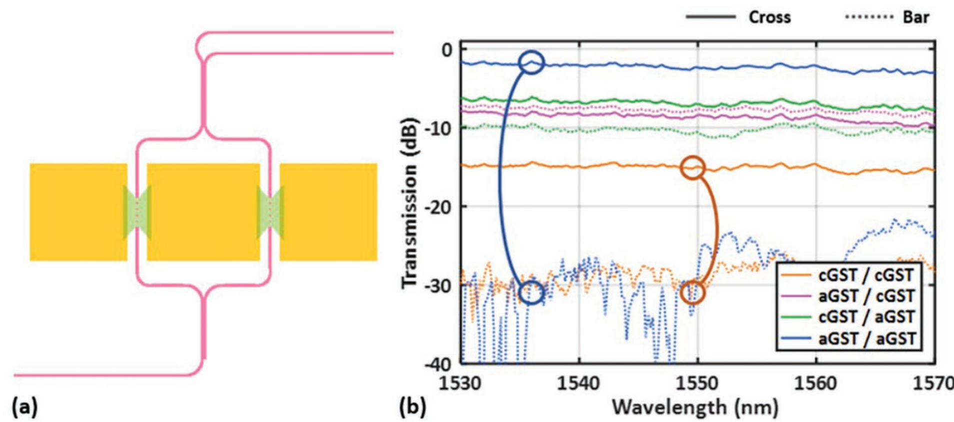

Figure 5. a) Schematic structure of the switching unit on the 2 × 2 balanced MZI. b) Transmission spectra in the four different permutations: the GSTs on both arms of the MZI are either in the fully amorphous or crystalline state. aGST (cGST): amorphous (crystalline) GST.

In addition, Figure 4b-d shows that the phase shift induced by the 10-µm-long GST is ≈0.4π, or, equivalently, ≈0.04 π µm^{-1}.

We further integrate two segmented switching units on a 2 × 2 balanced MZI, as shown in **Figure 5**a. The MZI contains two input and output ports and the two arms are equal in length. Fully reconfigurable transmission across a large bandwidth at the two output ports of the MZI can be achieved by continuously and independently changing the GST phases on the two arms, and thus changing the phase and loss differences. The core width of the MZI arm waveguide is chosen as 1 µm, which is beyond the singlemode condition of silicon photonic waveguides, thereby reducing the initial phase imbalance of the MZI due to fabrication variations, as proposed in our previous work.[46]

In order to demonstrate the versatile reconfigurations of this device, we characterized the transmission spectra at the two output ports when the GST segments on the two arms are switched between the fully amorphous and crystalline states, as shown in Figure 5b. When the GST segments on both arms are fully crystalline, the high optical loss causes large transmission loss in both arms, resulting in an EL of ≈15 dB at the cross port and the transmission <–30 dB at the bar port. When the GST segments on the two arms are fully amorphous and crystalline, respectively, the transmission spectra at the cross and bar ports are on the same order of magnitude due to the large loss difference between the two arms. When the GST segments on both arms are converted into the fully amorphous state, the low-loss property enables high optical transmission at the cross port in a broad wavelength range (≈40 nm) with an EL of ≈1.5 dB. Meanwhile, the power transmission is still maintained to <–30 dB at the bar port, indicating very well-balanced phase and loss between the two arms. In addition, by partially crystallizing or amorphizing the GST segments on the two arms, it is possible to achieve reversible and continuous multilevel tuning of the power transmissions at the two output ports of the MZI.

Furthermore, in order to fully elucidate the reconfigurable characteristics of the two output ports of the balanced MZI, we calculate the power transmissions at the two ports with arbitrary intermediate states of GSTs, as shown in **Figure 6**a-b. The calculations are based on the phase shift (0.04 π µm^{-1}) and loss contrast (1 dB µm^{-1}) of the GST obtained from the imbalanced MZI device described above. The transmissions at the two ports are symmetrically distributed with respect to the diagonal line from lower-left (aGST on both arms) to upper-right (cGST on both arms), indicating that ideally, the transmissions at the two output ports of the MZI remain unchanged when the GST states on the two arms are exactly swapped. The straight contour lines of the ER between the two output ports in Figure 6c indicate continuous sets of intermediate GST states on both arms that maintain a constant ER. By operating along any of these ER contour lines, the device can function as a variable attenuator at the cross port with a power tap at the bar port,[47] where the fixed tapping ratio is equal to the ER.

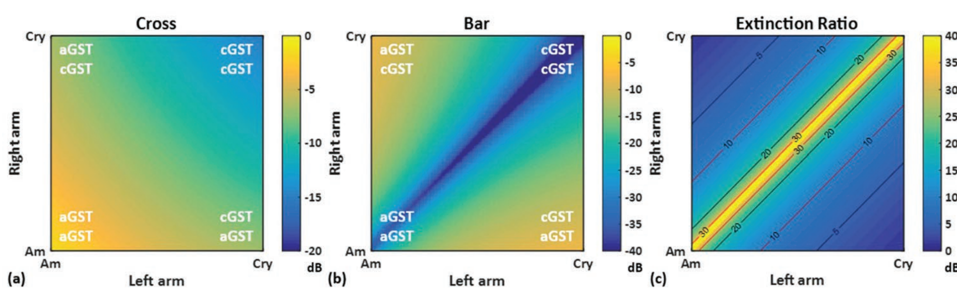

Figure 6. Calculated power transmissions of the 2 × 2 balanced MZI at the a) cross and b) bar port when GSTs on the two arms are in intermediate states. c) ER between the Cross and Bar port. The contours indicate constant ERs. aGST (cGST): amorphous (crystalline) GST. Am: amorphous; Cry: crystalline.

 © 2023 Wiley-VCH GmbH

21951071, 2023, 8, Downloaded from https://onlinelibrary.wiley.com/doi/10.1002/adom.202202748 by Westlake University, Wiley Online Library on [05/07/2023]. See the Terms and Conditions (https://onlinelibrary.wiley.com/terms-and-conditions) on Wiley Online Library for rules of use; OA articles are governed by the applicable Creative Commons License

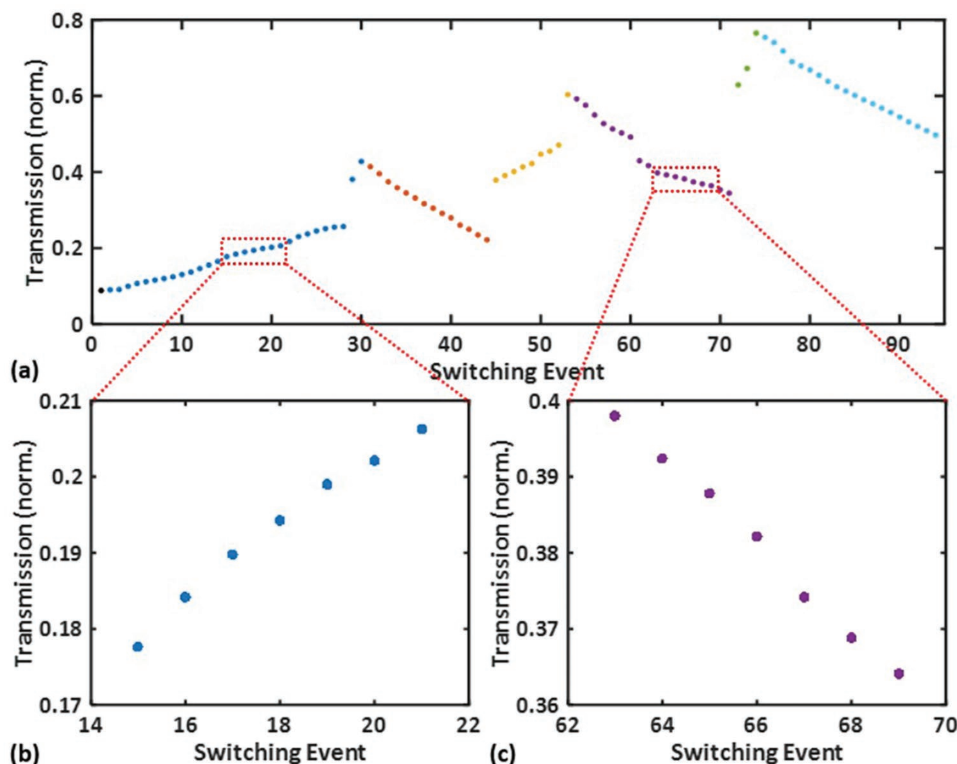

Figure 7. a) Transmission changes with pulse energies just above the threshold of the amorphization or crystallization process in the multi-stage phase transitions of GST. b) Zoomed-in transmission changes of the amorphization and c) crystallization processes.

Finally, to push the limit of multilevel switching capabilities of our segmented switching unit, we apply voltage pulses with varied pulse energies that are just sufficient to amorphize or crystallize the GST at different phase composition, and then measure the changes in the waveguide transmission. **Figure 7**a shows the transmission changes after each pulse, covering different intermediate states of GST within the full range between the fully amorphous and fully crystalline states. Each switching event corresponds to a phase change induced by applying a voltage pulse. Note that the abrupt changes near the Switching Events 30, 45, 52, 60, and 72 are intended to demonstrate both the amorphization and crystallization processes. The nonuniformity of the transmission change between adjacent levels arises from the stochastic nature of GST nucleation during phase transitions.[40] The minimum and maximum of the waveguide transmission are ≈0.08 and 0.8, respectively, corresponding to the fully crystalline and amorphous states. With the transmission change induced by a single pulse each time ≈0.01, the GST-loaded waveguide can produce up to 64 distinguishable switching levels, which corresponds to 6-bit precision. Furthermore, the transmission change in the marked regions in Figure 7b-c can be as low as ≈0.005, indicating the potential to reach 128 switching levels by fine-tuning the switching pulses. The precise and reversible control of the multi-stage phase transitions of GST is well suited for photonic computing, with a high computational precision of 6–7 bits.

Even though it is still quite challenging to precisely switch between two arbitrary levels with only a single pulse due to the stochastic nature of the phase transitions, a straightforward fine-tuning protocol can be used to achieve any transmission level within 6-bit precision. If the transmission of the computing unit needs to be adjusted to a low (high) level, the GST can be reset to a state with more crystalline (amorphous) composition, corresponding to a lower (higher) transmission than desired, then amorphization (crystallization) pulses with energies just above the threshold can be applied to gradually reach the desired transmission.

The above fine-tuning protocol, combined with the imbalanced and balanced MZI devices investigated above, enables high-precision programming and feedback control of photonic computing units, which is suitable for large-scale nonvolatile reconfigurable photonic computing networks.[20,27,48,49] These devices are especially well suited for the inference processes in deep neural networks (DNNs), which constitute a major part of the exponentially growing demand of computing power, but do not require frequent reconfigurations. Arguably, nonvolatile photonic circuit reconfiguration based on the PCM-loaded photonic waveguides is one of the most promising approaches to truly realize the long-anticipated ultralow power consumption of photonic computing, compared with their electronic counterparts, within compact and scalable footprints.

5. Conclusion

In conclusion, we have characterized and experimentally demonstrated precise and reversible nonvolatile multistage phase transitions of GST with In_2O_3 microheaters that are compatible

© 2023 Wiley-VCH GmbH

with diverse material platforms. Voltage pulses are applied to the In_2O_3 microheater which also functions as a protective layer to induce the amorphization and crystallization processes. The switching unit has been integrated with silicon photonic waveguides and MZIs. When controlling the phase change processes of GST, the loss contrast between the amorphous and crystalline states is measured to be ≈1 dB μm^{-1}, and the change in the real part of the refractive index induces a phase shift ≈0.04 π μm^{-1}. In particular, utilizing the segmented switching unit proposed in this paper, large temperature gradient of GST can be obtained and multi-stage phase change with up to 64 switching levels (i.e., 6-bit precision) is enabled with a total of 10-µm-long GST segments. It is even possible to reach 128 switching levels with further fine-tuning of the switching pulses. The precise multistage phase-change modulation is of great significance for the development of nonvolatile reconfigurable switching and variable attenuation devices.

Acknowledgements

This work is funded by the National Key Research and Development Program of China (2021YFB2801300), National Science Fund for Distinguished Young Scholars (61725503), National Natural Science Foundation of China (61961146003, 91950205, 92150302, 62175214, 62135010, 62105280), Leading Innovative and Entrepreneur Team Introduction Program of Zhejiang (2021R01001), Zhejiang Provincial Major Research and Development Program (2021C01199), Major Innovation Group Program of Zhejiang Province (LDT23F04012F05, LDT23F04015F05, LDT23F04014F01), Natural Science Foundation of Zhejiang Province (LZ22F050006), Fundamental Research Funds for the Central Universities (2021QNA5002), and Startup Foundation for Hundred-Talent Program of Zhejiang University. The authors thank ZJU Micro-Nano Fabrication Center, Westlake Center for Micro/Nano Fabrication and Instrumentation, and Dr. Wei Wang for the facility support and technical assistance.

Conflict of Interest

The authors declare no conflict of interest.

Data Availability Statement

The data that support the findings of this study are available from the corresponding author upon reasonable request.

Keywords

integrated photonics, nonvolatile, phase change materials, reconfigurable photonics, silicon photonics

Received: November 18, 2022
Revised: January 11, 2023
Published online: February 13, 2023

[1] A. H. Atabaki, S. Moazeni, F. Pavanello, H. Gevorgyan, J. Notaros, L. Alloatti, M. T. Wade, C. Sun, S. A. Kruger, H. Meng, K. Al Qubaisi, I. Wang, B. Zhang, A. Khilo, C. V. Baiocco, M. A. Popovic, V. M. Stojanovic, R. J. Ram, *Nature* **2018**, *556*, 349.
[2] X. Chen, M. M. Milosevic, S. Stankovic, S. Reynolds, T. D. Bucio, K. Li, D. J. Thomson, F. Gardes, G. T. Reed, *Proc. IEEE Inst. Electr. Electron. Eng.* **2018**, *106*, 2101.
[3] W. Bogaerts, D. Perez, J. Capmany, D. A. B. Miller, J. Poon, D. Englund, F. Morichetti, A. Melloni, *Nature* **2020**, *586*, 207.
[4] X. Xiao, R. Proietti, G. Liu, H. Lu, P. Fotouhi, S. Werner, Y. Zhang, S. J. B. Yoo, *IEEE J. Sel. Top. Quantum Electron.* **2020**, *26*, 3700210.
[5] Y. Xie, Y. Shi, L. Liu, J. Wang, R. Priti, G. Zhang, O. Liboiron-Ladouceur, D. Dai, *IEEE J. Sel. Top. Quantum Electron.* **2020**, *26*, 3600220.
[6] L. Qiao, W. Tang, T. Chu, *Sci. Rep.* **2017**, *7*, 42306.
[7] N. Dupuis, F. Doany, R. A. Budd, L. Schares, C. W. Baks, D. M. Kuchta, T. Hirokawa, B. G. Lee, *J. Lightwave Technol.* **2020**, *38*, 178.
[8] M. Wuttig, H. Bhaskaran, T. Taubner, *Nat. Photonics* **2017**, *11*, 465.
[9] Z. Fang, R. Chen, J. Zheng, A. Majumdar, *IEEE J. Sel. Top. Quantum Electron.* **2022**, *28*, 8200317.
[10] M. Stegmaier, C. Ríos, H. Bhaskaran, C. D. Wright, W. H. P. Pernice, *Adv. Opt. Mater.* **2017**, *5*, 1600346.
[11] C. Wu, H. Yu, H. Li, X. Zhang, I. Takeuchi, M. Li, *ACS Photonics* **2019**, *6*, 87.
[12] P. Xu, J. Zheng, J. K. Doylend, A. Majumdar, *ACS Photonics* **2019**, *6*, 553.
[13] H. Zhang, L. Zhou, L. Lu, J. Xu, N. Wang, H. Hu, B. M. A. Rahman, Z. Zhou, J. Chen, *ACS Photonics* **2019**, *6*, 2205.
[14] C. Zhang, M. Zhang, Y. Xie, Y. Shi, R. Kumar, R. R. Panepucci, D. Dai, *Photonics Res.* **2020**, *8*, 1171.
[15] J. Zheng, Z. Fang, C. Wu, S. Zhu, P. Xu, J. K. Doylend, S. Deshmukh, E. Pop, S. Dunham, M. Li, A. Majumdar, *Adv. Mater.* **2020**, *32*, 2001218.
[16] D. Wu, X. Yang, N. Wang, L. Lu, J. Chen, L. Zhou, B. M. A. Rahman, *Nanophotonics* **2022**, *11*, 3437.
[17] C. Ríos, M. Stegmaier, P. Hosseini, D. Wang, T. Scherer, C. D. Wright, H. Bhaskaran, W. H. P. Pernice, *Nat. Photonics* **2015**, *9*, 725.
[18] Z. Cheng, C. Rios, N. Youngblood, C. D. Wright, W. H. P. Pernice, H. Bhaskaran, *Adv. Mater.* **2018**, *30*, 1802435.
[19] X. Li, N. Youngblood, C. Ríos, Z. Cheng, C. D. Wright, W. H. P. Pernice, H. Bhaskaran, *Optica* **2019**, *6*, 1 .
[20] J. Feldmann, N. Youngblood, X. Li, C. D. Wright, H. Bhaskaran, W. H. P. Pernice, *IEEE J. Sel. Top. Quantum Electron.* **2020**, *26*, 8301807.
[21] X. Chen, Y. Xue, Y. Sun, J. Shen, S. Song, M. Zhu, Z. Song, Z. Cheng, P. Zhou, *Adv. Mater.* **2022**, 2203909.
[22] J. Feldmann, M. Stegmaier, N. Gruhler, C. Rios, H. Bhaskaran, C. D. Wright, W. H. P. Pernice, *Nat. Commun.* **2017**, *8*, 1256.
[23] C. Ríos, N. Youngblood, Z. Cheng, M. Le Gallo, H. P. Pernice Wolfram, C. D. Wright, A. Sebastian, H. Bhaskaran, *Sci. Adv.* **2019**, *5*, eaau5759.
[24] X. Li, N. Youngblood, Z. Cheng, S. G.-C. Carrillo, E. Gemo, W. H. P. Pernice, C. D. Wright, H. Bhaskaran, *Optica* **2020**, *7*, 218.
[25] Z. Cheng, C. Ríos, H. P. Pernice Wolfram, C. D. Wright, H. Bhaskaran, *Sci. Adv.* **2017**, *3*, e1700160.
[26] J. Feldmann, N. Youngblood, C. D. Wright, H. Bhaskaran, W. H. P. Pernice, *Nature* **2019**, *569*, 208.
[27] J. Feldmann, N. Youngblood, M. Karpov, H. Gehring, X. Li, M. Stappers, M. L.e Gallo, X. Fu, A. Lukashchuk, A. S. Raja, J. Liu, C. D. Wright, A. Sebastian, T. J. Kippenberg, W. H. P. Pernice, H. Bhaskaran, *Nature* **2021**, *589*, 52.
[28] C. Wu, H. Yu, S. Lee, R. Peng, I. Takeuchi, M. Li, *Nat. Commun.* **2021**, *12*, 96.
[29] S. Abdollahramezani, O. Hemmatyar, H. Taghinejad, A. Krasnok, Y. Kiarashinejad, M. Zandehshahvar, A. Alù, A. Adibi, *Nanophotonics* **2020**, *9*, 1189.

 © 2023 Wiley-VCH GmbH

21951071, 2023, 8, Downloaded from https://onlinelibrary.wiley.com/doi/10.1002/adom.202202748 by Westlake University, Wiley Online Library on [05/07/2023]. See the Terms and Conditions (https://onlinelibrary.wiley.com/terms-and-conditions) on Wiley Online Library for rules of use; OA articles are governed by the applicable Creative Commons License

[30] R. Chen, Z. Fang, F. Miller, H. Rarick, J. E. Fröch, A. Majumdar, *ACS Photonics* **2022**, *9*, 3181.
[31] M. Stegmaier, C. Ríos, H. Bhaskaran, W. H. P. Pernice, *ACS Photonics* **2016**, *3*, 828.
[32] J. Zheng, S. Zhu, P. Xu, S. Dunham, A. Majumdar, *ACS Appl. Mater. Interfaces* **2020**, *12*, 21827.
[33] J. Parra, I. Olivares, A. Brimont, P. Sanchis, *Laser Photonics Rev.* **2021**, *15*, 2000501 .
[34] N. Farmakidis, N. Youngblood, X. Li, J. Tan, L. Swett Jacob, Z. Cheng, C. D. Wright, H. P. Pernice Wolfram, H. Bhaskaran, *Sci. Adv.* **2019**, *5*, eaaw2687.
[35] N. Farmakidis, N. Youngblood, J. S. Lee, J. Feldmann, A. Lodi, X. Li, S. Aggarwal, W. Zhou, L. Bogani, W. H. Pernice, C. D. Wright, H. Bhaskaran, *Adv. Sci.* **2022**, *9*, 2200383.
[36] Y. Zhang, C. Ríos, M. Y. Shalaginov, M. Li, A. Majumdar, T. Gu, J. Hu, *Appl. Phys. Lett.* **2021**, *118*, 210501.
[37] H. Zhang, L. Zhou, J. Xu, N. Wang, H. Hu, L. Lu, B. M. A. Rahman, J. Chen, *Sci. Bull.* **2019**, *64*, 782.
[38] C. Ríos, Q. Du, Y. Zhang, C. Popescu, M. Y. Shalaginov, P. Miller, C. Roberts, M. Kang, K. A. Richardson, T. Gu, S. A. Vitale, J. Hu, *Photonix* **2022**, *3*, 26.
[39] R. Chen, Z. Fang, J. E. Fröch, P. Xu, J. Zheng, A. Majumdar, *ACS Photonics* **2022**, *9*, 2142.
[40] C. Ríos, Y. Zhang, M. Y. Shalaginov, S. Deckoff-Jones, H. Wang, S. An, H. Zhang, M. Kang, K. A. Richardson, C. Roberts, J. B. Chou, V. Liberman, S. A. Vitale, J. Kong, T. Gu, J. Hu, *Adv. Photonics Res.* **2020**, *2*, 2000034.
[41] Z. Fang, R. Chen, J. Zheng, A. I. Khan, K. M. Neilson, S. J. Geiger, D. M. Callahan, M. G. Moebius, A. Saxena, M. E. Chen, C. Rios, J. Hu, E. Pop, A. Majumdar, *Nat. Nanotechnol.* **2022**, *17*, 842.
[42] K. Kato, M. Kuwahara, H. Kawashima, T. Tsuruoka, H. Tsuda, *Appl. Phys. Express* **2017**, *10*, 072201.
[43] Z. Fang, J. Zheng, A. Saxena, J. Whitehead, Y. Chen, A. Majumdar, *Adv. Opt. Mater.* **2021**, *9*, 2002049.
[44] H. Taghinejad, S. Abdollahramezani, A. A. Eftekhar, T. Fan, A. H. Hosseinnia, O. Hemmatyar, A. E. Dorche, A. Gallmon, A. Adibi, *Opt. Express* **2021**, *29*, 20449.
[45] C. Rios, M. Stegmaier, Z. Cheng, N. Youngblood, C. D. Wright, W. H. P. Pernice, H. Bhaskaran, *Opt. Mater. Express* **2018**, *8*, 2455.
[46] L. Song, T. Chen, W. Liu, H. Liu, Y. Peng, Z. Yu, H. Li, Y. Shi, D. Dai, *Photonics Res.* **2022**, *10*, 793.
[47] Y. Zhang, Q. Zhang, C. Ríos, M. Y. Shalaginov, J. B. Chou, C. Roberts, P. Miller, P. Robinson, V. Liberman, M. Kang, K. A. Richardson, T. Gu, S. A. Vitale, J. Hu, *ACS Photonics* **2021**, *8*, 1903.
[48] W. Zhang, J. Yao, *Nat. Commun.* **2020**, *11*, 406.
[49] K. Liao, Y. Chen, Z. Yu, X. Hu, X. Wang, C. Lu, H. Lin, Q. Du, J. Hu, Q. Gong, *Opto-Electron. Adv.* **2021**, *4*, 200060.

© 2023 Wiley-VCH GmbH

21951071, 2023, 8, Downloaded from https://onlinelibrary.wiley.com/doi/10.1002/adom.202202748 by Westlake University, Wiley Online Library on [05/07/2023]. See the Terms and Conditions (https://onlinelibrary.wiley.com/terms-and-conditions) on Wiley Online Library for rules of use; OA articles are governed by the applicable Creative Commons License